Scaling Behavior in Anisotropic Hele-Shaw Flow

Robert Almgren
Department of Mathematics, The University of Chicago, 5734 S. University Avenue, Chicago, Illinois 60637

Wei-Shen Dai*
The James Franck Institute, The University of Chicago, Chicago, Illinois 60637

Vincent Hakim
Laboratoire de Physique Statistique, Ecole Normale Supérieure, 24 rue Lhomond, 75231 Paris Cedex 05, France
(Received 1 April 1993)

We find the self-similar scaling behavior $x \sim t^{3/5}, y \sim t^{2/5}$ for the arms which form in radial Hele-Shaw flow with anisotropic surface energy, where x is the longitudinal and y is the transverse coordinate of each primary finger. We first observe this by direct numerical simulation using a boundary-integral method. Then we analytically derive the scaling law and the full asymptotic shape, by combining a simple boundary-layer analysis with previous results on velocity selection.

PACS numbers: 47.15.Hg, 47.20.Hw, 68.10.−m

The equations of Hele-Shaw flow are quite well known. In the region exterior to a growing bubble or seed in the plane there is a harmonic scalar potential field $\phi(\mathbf{x},t)$ satisfying the Laplace equation with prescribed far-field behavior

$$\Delta\phi=0, \quad \phi(\mathbf{x},t)\sim\ln|\mathbf{x}|, \quad |\mathbf{x}|\to\infty . \tag{1}$$

The local normal velocity of the interface $\Gamma(t)$ is given by the consistency condition

$$V_n=\frac{\partial\phi}{\partial n} . \tag{2}$$

We have chosen our length and time scales so that the rate of change of area of the bubble is 2π.

For the derivation of this model, the reader may consult a number of sources. The most popular way in which it arises is in describing viscous fluid flow in a Hele-Shaw cell, that is, flow between two closely spaced flat plates (see [1,2]). Then ϕ is the negative of the pressure, the fluid velocity is $\mathbf{v}=\nabla\phi$, and Eq. (1) expresses incompressibility of the fluid, together with a constant volumetric injection rate. We neglect complicated three-dimensional details of the fluid-air interface.

The same model also describes growth of a solid crystal by solidification from its melt [2], in the "quasistatic" limit of small undercooling or impurity concentration, so that the growth rate of the seed is slow compared to the rate of adjustment of the diffusion field, and Eq. (1) replaces the diffusion equation.

We complete the system (1,2) by requiring ϕ to satisfy an anisotropic local-equilibrium condition on Γ:

$$\phi|_\Gamma=d_0(1-\epsilon\cos m\theta)\mathcal{K} , \tag{3}$$

where d_0 is an effective surface tension parameter, and $\mathcal{K}$ is the local geometric curvature of Γ, positive where the bubble or seed is convex. We have chosen a simple form for the anisotropy, described only by its strength ϵ and its symmetry m. The angle θ is the orientation of the outward normal relative to a fixed direction such as the x axis. In this Letter we shall always take $m=4$. In order to explore the long-time scaling behavior of this system for $m=4$, we may fix the value of d_0, and vary only the single parameter ϵ.

In the Hele-Shaw fluid system, attention is most often restricted to the isotropic case, $\epsilon=0$. Anisotropy may be introduced by engraving a regular grid on the plates [3]; it has been shown [4] that this does not affect the bulk condition (1), but certainly does perturb the boundary condition to something like (3).

In solidification, Eq. (3) is the Gibbs-Thomson condition (see [2,5]). In this case the anisotropy is very natural; it comes from the existence of a crystal lattice structure inside the growing seed.

Numerical method.—We have adapted the boundary-integral method of [6] for isotropic Hele-Shaw flow to solve the system (1)–(3), with improvements developed in [7]. The boundary-integral formulation has been used for isotropic Hele-Shaw flow in [8], and a related method for anisotropic crystal growth in [4,9]. In this formulation, the interface is written as a complex function $z(p)$, periodic with period 2π in the real parameter p, and the complex potential $w(x+iy)$, of which ϕ is the real part, is written

$$w(\eta)=\ln\eta+\frac{1}{2\pi i}\int_0^{2\pi}\gamma(p)\ln[\eta-z(p)]dp .$$

The contribution from the interface is represented in terms of a real-valued vortex sheet strength $\gamma(p)$ with zero mean. The boundary condition (3) leads [6] to the linear integral equation

$$\gamma(p)=-2\,\mathrm{Re}\left\{\frac{z_p(p)}{2\pi i}P\int_0^{2\pi}\frac{\gamma(p')}{z(p)-z(p')}dp'\right\} -2\,\mathrm{Re}\left\{\frac{z_p(p)}{z(p)}\right\}-2d_0\frac{d}{dp}\{[1-\epsilon\cos\theta(p)]\mathcal{K}(p)\} \tag{4}$$

0031-9007/93/71(21)/3461(4)$06.00

for $\gamma(p)$, where $P\int$ denotes the Cauchy principal-value integral. We approximate principal-value integrals with spectra accuracy, using alternate-point quadrature formulas introduced in [10] and first used for vortex sheet computations in [11]. For a given instantaneous interface configuration $z(p)$, (4) is solved by iteration; as in [6], convergence of the iteration is accelerated up to tenfold by using cyclic Chebyshev semi-iterative techniques [12].

The complex conjugate velocity field $Q^* = dw/dz = u - iv$ at a point $z(p)$ on the interface is

$$\lim_{\eta \to z} Q^*(\eta) = \frac{1}{z(p)} + \frac{1}{2}\frac{\gamma(p)}{z_p(p)} + \frac{1}{2\pi i} P\int_0^{2\pi} \frac{\gamma(p')}{z(p)-z(p')}dp' .$$

As in [4,9], we use as dynamic variables the local orientation $\theta(p)$ and the arc length $s(p)$, and we maintain an equal-arclength representation; that is, $s_p = L/2\pi$, where $L(t)$ is the total length of the interface. The local velocity is written in normal and tangential components $Q(p) = U(p)\mathbf{n} + V(p)\mathbf{t}$, and $\theta(p,t)$ and $L(t)$ are updated according to

$$\frac{\partial \theta}{\partial t} = \frac{1}{s_p} U_p + \mathcal{K}\tilde{V} ,$$
$$\frac{dL}{dt} = s_p \int_0^{2\pi} U(p)\mathcal{K}(p)dp , \tag{5}$$

where $\tilde{V}(p)$ is a modified tangential velocity [4,7], determined to maintain the equal-arclength representation.

The advantage of this representation is that we may use knowledge obtained in [7] of the behavior of the high Fourier modes of (5) for $\epsilon = 0$ to reduce the stiffness of the associated system of ordinary differential equations: if $\theta(p,t) = \sum_{n=1}^{N} \theta_n(t) e^{inp}$, then $d\theta_n/dt$ for large n is nearly linear in θ_n with coefficient proportional to $-d_0|n|^3$. In applying this result to our anisotropic case, we use only the mean value of the surface tension, d_0, which reduces somewhat the effectiveness of our code at large anisotropies. The terms remaining after extracting the linear part are advanced with a second-order Adams-Bashforth method; since spectral accuracy is achieved in the space discretization, the time stepping is the only significant contribution to the formal truncation error of the scheme.

Filtering techniques [13] are used to prevent growth of roundoff error in the high Fourier modes; convergence of a scheme including such filtering has recently been proven for isotropic Hele-Shaw flow [14]. The number of points N is doubled whenever significant amplitude appears in modes θ_n for $n > N/2$. The code enforces both fourfold rotational and bilateral reflection symmetries.

For all our computations, we take $d_0 = 0.001$, in order to obtain interesting behavior when the bubble or seed is of sizes $O(1)$. We use as initial condition a circle of radius 0.1; at early times the seed remains roughly round, of radius $r \approx \sqrt{r_0^2 + 2t}$. When the seed reaches a large enough size, instability sets in [15], and arms begin to form. The initial perturbation which "kicks off" the instability is provided by the anisotropy of the surface tension. For $R \approx 0.2$, the linear growth rate of the Fourier modes has a maximum very near the eighth mode; thus even though the perturbation is fourfold symmetric, bumps form at the intermediate orientations as well, generating secondary arms. In the later nonlinear regime, the secondary arms grow more slowly than the primary since they are not favored by the surface energy anisotropy.

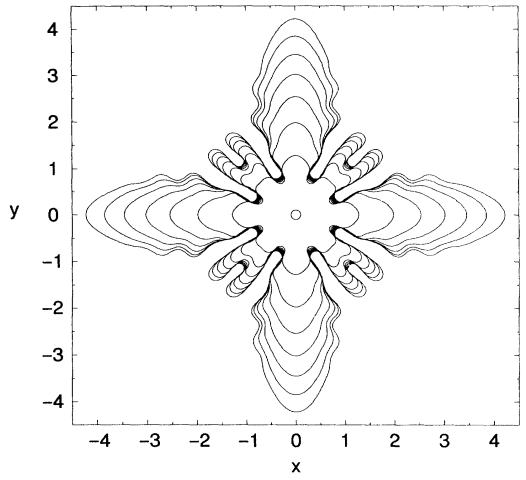

FIG. 1. $\epsilon = 0.1$, $t = 0$ to 3.5, $\Delta t = 0.5$.

In Figs. 1 and 2, we show the full computations, for $\epsilon = 0.1$ and 0.5, respectively. For $\epsilon = 0.1$, the computational time step $\Delta t = 5 \times 10^{-4}$; for $\epsilon = 0.5$, $\Delta t = 10^{-4}$ initially, increased to 2×10^{-4} for $t \geq 1$. The number of computational nodes on one-quarter of the interface was 1024 initially, increased to 2048 for $\epsilon = 0.5$ at $t = 0.61$.

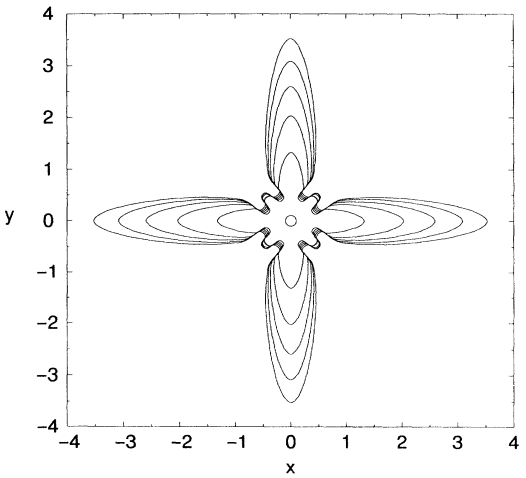

FIG. 2. $\epsilon = 0.5$, $t = 0$ to 1.5, $\Delta t = 0.3$.

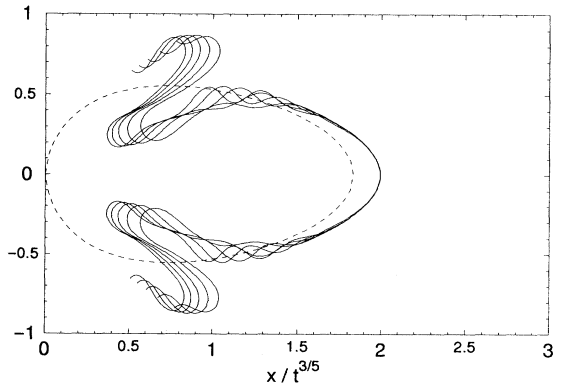

FIG. 3. Scaled $\epsilon=0.1$, $t=1.5$ to 3.5, $\Delta t=0.5$.

For $\epsilon=0.5$ (Fig. 2), the aspect ratio of the primary fingers is small and the tips advance rapidly; the secondary fingers are strongly unfavored and their growth is suppressed. For $\epsilon=0.1$ (Fig. 1), the secondary fingers keep growing and their tips split; for both of these values of ϵ the primary fingers are apparently stabilized against tip splitting. Our result for $\epsilon=0.1$ is qualitatively very similar to the corresponding one presented in [4]; we do not know of any other computations which have used ϵ as large as 0.5. We believe that our computations are long enough to show the long-time asymptotic behavior of the overall shapes of the primary fingers.

In order to describe the structure of these shapes, in Figs. 3 and 4 we have displayed the same data for one quarter of the interface including one primary finger, but with x (the longitudinal coordinate) and y (the transverse coordinate) scaled by complementary powers of t. The axes are $x/t^{3/5}$ and $y/t^{2/5}$, where the exponent $\alpha=3/5$ is determined in the following section; the sum of the exponents must be 1 since the area grows linearly in time. We see very clear self-similar scaling behavior, after initial transient periods which are not plotted. That is, our computations indicate that, up to changes in parametrization, the long-time behavior of the primary fingers is apparently of the form

$$x(p,t,\epsilon)=t^{3/5}x_0(p,\epsilon),\quad y(p,t,\epsilon)=t^{2/5}y_0(p,\epsilon),$$

for some base profile (x_0,y_0) which may depend on ϵ. This base profile is the "egg" shape in Figs. 3 and 4 which is very well-defined around the tip, and is better and better delineated near the back as time advances.

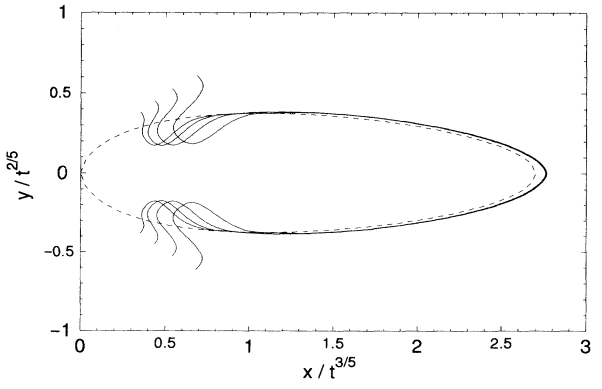

FIG. 4. Scaled $\epsilon=0.5$, $t=0.6$ to 1.5, $\Delta t=0.3$.

We have performed the same computations with half the time step for $\epsilon=0.5$, obtaining agreement with these solutions to four decimal places at $t=0.6$.

Scaling and selection theory.—The above scaling is very different from the $t^{1/2}$ behavior conjectured in [16]. We now show how it may be understood by analyzing the growing profile on two different length scales in a boundary layerlike fashion: The outer length scale is characteristic of the whole object, while the inner scale is that of the tip radius of curvature. We make the assumption, based on our numerical results, that the tip position is asymptotically of the form $x\sim At^{\alpha}$, $\frac{1}{2}<\alpha<1$; then, as explained above, y must scale like $t^{1-\alpha}$. We show how to determine the exponent α, the coefficient A, and the entire asymptotic egg shapes.

First, we show how the scaling exponent α is determined by matching between the two length scales. In the inner scale, d_0 is the only dimensional parameter which controls the selection of the tip shape. Since ϕ, being a rate of change of area, has dimension L^2/T, the dimension of d_0 is L^3/T [see Eq. (3)]. Therefore, as in [2,17], the result of selection theory applied to the tip must be a law giving the dimensionless number ρ^2V/d_0 as a function of the anisotropy ϵ, where ρ denotes the tip radius of curvature and V the instantaneous velocity. Since $V\sim dx/dt\sim t^{\alpha-1}$ and $\rho\sim(d^2x/dy^2)^{-1}\sim t^{2-3\alpha}$, we see $\rho^2V\sim t^{3-5\alpha}$, and constancy of ρ^2V requires $\alpha=3/5$.

Now we determine the growing self-similar shape in terms of A and α. At large times, since the width of each arm becomes small compared to its length, the field around the crystal may be determined by replacing the fingers by line segments, and the overall shape by a cross in the complex plane $z=x+iy$ with vertices at $\pm R(t)$, $\pm iR(t)$, with $R(t)=At^{\alpha}$. The potential $\phi(z)$, with $\phi=0$ on the surface of the cross and having the far-field behavior specified in Eq. (1), may be determined by conformal mapping onto a circle as in [18]; the result is

$$w=\phi+i\psi=\tfrac{1}{2}\cosh^{-1}\left(\frac{z}{R}\right)^2,\quad \frac{dw}{dz}=\frac{z}{\sqrt{z^4-R^4}}.$$

By Eq. (2), the lateral velocity of the sides of the finger is given by dw/dz; focusing attention at a fixed point x on the top side of the rightward-pointing finger, we have

$$\frac{dy}{dt}=\frac{x}{\sqrt{x_{\rm tip}^4-x^4}},\quad 0<x<x_{\rm tip}(t)=At^{3/5}.$$

We therefore obtain the complete asymptotic shape

$$y(x,t)=t^{2/5}\frac{5}{3A}\left[\frac{x}{x_{\rm tip}}\right]^{2/3}\int_{x/x_{\rm tip}}^{1}\frac{ds}{s^{2/3}\sqrt{1-s^4}}. \quad (6)$$

Only the parameter A remains to be determined.

It may be seen from Eq. (6) that the tip radius of curvature scales as $t^{1/5}$. In local coordinates $x_{\rm tip}-x=t^{1/5}\xi, y=t^{1/5}\eta$, Eq. (6) can be expanded as

$$\xi=\left[\frac{3}{5}\right]^2 A^3\eta^2+b_1\frac{\eta^4}{t^{2/5}}+\cdots+b_n\frac{\eta^{2n+2}}{t^{2n/5}}+\cdots.$$

So as time increases, the tip shape appears as a parabola on ever increasing lengths when measured on the scale of the tip radius of curvature. The effect of a nonzero d_0 [Eq. (3)] on this parabola can be analyzed in a standard manner [2,17] by writing an integral equation for the tip shape evolution. Searching for this shape in the form $\xi=\xi(\eta,t)$, we see that the $t^{1/5}$ contributes a negligible amount to the local normal velocity at a fixed η, as compared to the tip velocity $\dot{x}_{\rm tip}(t)$. So the result would be the same equation as for a parabola of constant shape propagating at constant speed, with the whole time dependence included in the product $\rho(t)^2V(t)$. We may therefore use directly the numerical results presented in [17]. In their notation,

$$\frac{\rho(t)^2V(t)}{d_0}=\tfrac{1}{8}C(\epsilon),$$

using the fact that the selected dimensionless parameter ρ^2V/d_0 is 2 times smaller [19] for the one-sided model than for the symmetric model of [17]. Since $\rho=\frac{1}{2}(5/3)^2A^{-3}t^{1/5}$ and $V=(3/5)At^{-2/5}$, this determines the only remaining parameter $A(\epsilon)$ in Eq. (6):

$$A(\epsilon)=\left[\frac{250}{27d_0C(\epsilon)}\right]^{1/5}.$$

Using the values $C(0.5)=64.5$ and $C(0.1)=449.5$ presented in [17], we obtain $A(0.5)=2.70$ and $A(0.1)=1.83$. The corresponding analytical curves are compared with the numerical results in Figs. 3 and 4. We emphasize that the dashed lines are completely determined by the analysis above, with no free parameters. For $\epsilon=0.5$, the fit is very good. In Fig. 3, for $\epsilon=0.1$, the fit to the calculated solution is not as good, although the solution exhibits a clear $t^{3/5}\times t^{2/5}$ scaling. One reason for this discrepancy may be because across the time we have been able to compute, the secondary arms are absorbing a constant fraction of the volume flux.

In conclusion, we point out that this self-similar behavior is relevant not only for viscous fingering, but also for dendritic growth at small undercooling. There, it should exist as an intermediate-time asymptotic regime, which holds as long as the diffusion length is larger than the whole structure size, before the subsequent crossover to the classical constant-velocity regime. Finally, it will be very interesting to see how sidebranching transforms this compact self-similar structure into an anisotropic fractal.

R.A. was partially supported by NSF DMS-9007246; W.D. was supported by NSF DMR 9115595. We thank Mike Shelley and Efim Brener for helpful discussions. We thank the Geometry Center in Minneapolis for sharing supercomputer time. Much of this work was done during a visit of R.A. to the Ecole Normale Supérieure at the generous invitation of Martine Ben Amar; we thank it and her for making it possible. The L.P.S. is "CNRS-URA1306 associé" with the Universities of Paris VI and VII.

*Current address: Electrotechnical Laboratory, Supermolecular Division, Tsukuba, Ibaraki 305, Japan.

[1] D. Bensimon *et al.*, Rev. Mod. Phys. **58**, 977 (1986).
[2] D. A. Kessler, J. Koplik, and H. Levine, Adv. Phys. **37**, 255 (1988); J. S. Langer, in *Chance and Matter*, edited by J. Souletie, J. Vannimenus, and R. Stora (Elsevier Science Publishers, New York, 1987), pp. 629–711.
[3] E. Ben-Jacob *et al.*, Phys. Rev. Lett. **55**, 1315 (1985).
[4] S. K. Sarkar and D. Jasnow, Phys. Rev. A **39**, 5299 (1989).
[5] R. Almgren, J. Comput. Phys. **106**, 337 (1993).
[6] W. Dai and M. J. Shelley (unpublished).
[7] T. Hou, J. Lowengrub, and M. Shelley (unpublished).
[8] A. J. DeGregoria and L. W. Schwartz, J. Fluid Mech. **164**, 383 (1986).
[9] D. A. Kessler, J. Koplik, and H. Levine, Phys. Rev. A **30**, 2820 (1984).
[10] A. Sidi and M. Israeli, J. Sci. Comput. **3**, 201 (1988).
[11] M. J. Shelley, J. Fluid Mech. **244**, 493 (1992).
[12] W. F. Ames, *Numerical Methods for Partial Differential Equations* (Academic Press, New York, 1977).
[13] R. Krasny, J. Fluid Mech. **167**, 65 (1986); T. Hou, J. Lowengrub, and R. Caflisch (unpublished).
[14] T. Beale, T. Hou, and J. Lowengrub (unpublished).
[15] W. W. Mullins and R. F. Sekerka, J. Appl. Phys. **34**, 323 (1963).
[16] M. Ben Amar, Europhys. Lett. **16**, 367 (1991).
[17] M. Ben Amar and Y. Pomeau, Europhys. Lett. **2**, 307 (1986).
[18] J.-P. Eckmann *et al.*, Phys. Rev. A **39**, 3185 (1989); B. Derrida and V. Hakim, Phys. Rev. A **45**, 8759 (1992), and references therein.
[19] C. Misbah, J. Phys. (Paris) **48**, 1265 (1987).